ADVANCED ENGINEERING MATERIALS
www.aem-journal.com

A Critical Appraisal of the Instrumented Indentation Technique and Profilometry-Based Inverse Finite Element Method Indentation Plastometry for Obtaining Stress–Strain Curves

*Jimmy E. Campbell, Hannah Zhang, Max Burley, Mark Gee, Antony Thomas Fry, James Dean, and Trevor William Clyne**

A comparison is presented between conventional tensile stress-strain curves and those obtained via two methodologies based on (spherical) indentation. The first, termed Instrumented Indentation Technique (IIT), involves conversion of load-displacement data to stress-strain curves via analytical expressions. This has been done using loads below 1 N ("nano") and in the kN range ("macro"). The other procedure, termed profilometry-based indentation plastometry (PIP), is based on repeated finite element method (FEM) simulation, using the residual indent profile as the target outcome and obtaining the best fit set of parameter values in a constitutive stress-strain law. This has been done on a macro scale only. The data from nano-IIT tend to be very noisy and variable, whereas those from macro-IIT are more reproducible and less noisy. With one of the two empirical formulations employed, the agreement of the macro-IIT with experiment is close to being acceptable for the work hardening characteristics, although inferred values of the yield stress are in poor agreement with those from tensile testing. In contrast to this, the PIP procedure provides outcomes that are in close agreement with those from tensile testing, concerning both yield stress and work hardening. The causes of this are explored and discussed.

1. Introduction

1.1. General Background

A longstanding aim is to obtain reliable stress–strain curves, of the type that results from conventional tensile testing, via the much simpler and more convenient operation of pushing a hard indenter into a free surface. This interest extends back almost to the development[1,2] of the first indentation-based hardness tester (Brinell) in 1900. The meaning of hardness, and the nature of the stress and strain fields generated in samples during different types of hardness test, was studied in some depth during the 1950s and 1960s, with Tabor's contributions[3,4] being prominent. It was recognized that, provided work hardening could be ignored, i.e., for an "elastic—perfectly plastic" material, then an approximate value for the yield stress could be obtained from a hardness number by simply multiplying it by a constant factor. However, in practice, work hardening is a key part of metal plasticity and in general this is not a reliable or useful operation.

Development, from around 1990, of instrumented indentation equipment, with load and penetration depth continually monitored, raised hopes that these much richer data sets could be used to extract stress–strain relationships. This development was in most cases associated with refinement of the scale of the test. Such refinement actually began in 1924 with introduction of the Vickers hardness test, which typically involves loads of a few tens or hundreds of *N* (≈1–30 kg f), creating indents with diameters of a few tens or hundreds of μm and depths of ≈1–30 μm. This may be compared with a load of 30 kN, and indents a few mm in diameter, with the Brinell test. However, from the start, instrumented indentation was often carried out with loads in the mN range and depths in the nm range, such that they were described as nanoindenters. This had various attractions, but it has somewhat complicated the development of a capability for extracting reliable stress–strain curves.

The reason for this is that, for any type of test, the region being plastically deformed must be large enough for its response to

Dr. J. E. Campbell, Dr. M. Burley, Dr. J. Dean, Prof. T. W. Clyne
Plastometrex Ltd
204 Science Park, Milton Road, Cambridge CB2 0GZ, UK
E-mail: b.clyne@plastometrex.com

Dr. H. Zhang, Prof. M. Gee, Dr. A. T. Fry
National Physical Laboratory
Hampton Road, Teddington TW11 0LW, UK

Prof. T. W. Clyne
Department of Materials Science
27 Charles Babbage Road, Cambridge CB3 0FS, UK

The ORCID identification number(s) for the author(s) of this article can be found under https://doi.org/10.1002/adem.202001496.

DOI: 10.1002/adem.202001496

reflect that of the bulk. In particular, for a typical (polycrystalline) metal, a "many-grained" volume must be deformed, as the plastic response of the bulk is influenced by microstructural features that include the grain size and shape, the crystallographic texture, and the grain boundary structure (influencing the ease of intergranular sliding and grain rotation). Indenting within a single grain, or even deforming a small assembly of grains, is unlikely to allow the stress–strain relationship of the bulk to be accurately obtained. As typical grain sizes are in the broad range of a few microns up to a few hundred microns, creating indents of submicron depth, with diameters of no more than a few microns, does not in general involve deformation of a representative volume. Separating this potential source of error from the inherent reliability of any procedure for obtaining a stress–strain curve from indentation data has proved troublesome.

Leaving this issue aside for the moment, two main approaches have been adopted for extraction of stress–strain curves from indentation data. The first, commonly termed the "Instrumented Indentation Technique" (IIT), seeks to convert load-displacement data directly to stress–strain curves, using analytical relationships. This involves gross simplifications concerning actual stress and strain fields under the indenter, although it is attractive in terms of the ease and speed of obtaining the final outcome. The second is a more rigorous approach, although inevitably more cumbersome. It is based on iterative finite element method (FEM) simulation of the indentation process, systematically changing the values of the parameters in a constitutive plasticity law until optimum agreement is reached between a measured and a modeled outcome—either the load-displacement plot or the residual indent profile. The latter is now often preferred[5–8] and in this case the procedure is termed "Profilometry-based Inverse FEM Indentation Plastometry" (PIP). These two procedures are described in detail later, after some comments regarding indenter shape.

1.2. Indenter Shape

The basic choice is between a sphere and a more complex ("sharp") shape. Although the Brinell indenter is a sphere, the Vickers indenter is a square pyramid (with the included angle between opposite faces having the relatively large value of 136°). An attraction of this is that, for a given load and sample material, it creates an indent with a large diameter, i.e., it reduces the load requirements for creating an indent that is large enough to measure readily. There is also the point that most sharp indenters are self-similar. For such shapes, the geometry of an axial section through the indenter (and sample) remains unchanged, apart from its scale, as penetration occurs. Characteristics of such shapes include the fact that the ratio of contact area to depth is constant (for a given shape, and ignoring effects of pile-up or sink-in around the indenter). There is thus no scale effect. This is sometimes considered advantageous for certain types of analysis, mainly those based on load-displacement data. Most indenter shapes in which the sides are linear in an axial section are self-similar. The most commonly encountered indenter shape that is not self-similar is that of a sphere, for which the ratio of contact area to depth is given by $2\pi R$, where R is the radius of the indenter.

Nevertheless, there are in practice strong incentives to use spherical indenters. These advantages have been highlighted a number of times.[9–13] One motivation is that a sphere is much less prone to become damaged than are shapes having edges or points. It is also easier to specify and manufacture. There is also reduced risk with spheres of encountering the computational problems that can arise with simulation of behavior in regions of high local curvature (edges or points). Finally, at least with (approximately) isotropic materials, a spherical indenter allows the FEM modeling to be radially symmetric (2D), which is not possible with most shaped indenters. The potential need for very large numbers of iterative FEM runs (in PIP procedures) makes this a more significant issue than it would otherwise be. Moreover, even for IIT procedures (which do not involve FEM), the use of sharp indenters leads to unhelpful complexity. Unfortunately, a lot of work in this area has been done both on a very fine scale and with sharp indenters. The associated errors mean that much of it has to be discounted. The current work is focused entirely on spherical indenters (although covering a wide range of length scales).

1.3. IIT Procedures

There have been many publications in which analytical approaches to the conversion of load-displacement data to stress–strain curves have been presented and/or used. Even if attention is limited to spherical indenters, the number of articles of this type is large.[14–27] The procedure may or may not involve representing the complete (plastic) stress–strain curve with an analytical expression. It may also be noted that methodologies have been suggested[28–31] that are based on the use of neural network techniques (essentially curve-fitting operations) to correlate load-displacement characteristics with corresponding stress–strain curves. These are conceptually related to IIT procedures, and they rely on an essentially empirical algorithm of some sort, but their independent appraisal is difficult to tackle and they are not further considered here.

Most IIT methodologies are based on repeated interruption, partial unloading and reloading during the test. Instrumented indentation systems are commonly run under some kind of software control, so this is easy to implement automatically. The "stiffness" of the system, S (in $\mathrm{N\,m^{-1}}$), which is given by the load, P, over the penetration, h, is evaluated at the points where (elastic) unloading is carried out. As h is increased, S rises (as greater amounts of the sample are being deformed). Each of these operations is converted in some way to a single point in (true) stress–strain space. This is usually done by obtaining "effective" (or "representative") values of both the stress and the strain acting within the sample at each stage. This inevitably requires gross approximations, not only because both stress and strain actually vary widely with location under an indenter but also because it is the deviatoric (von Mises) values of both that are required for this purpose and these are not equal to the values acting in the loading direction (as both stress and strain fields are highly multiaxial during indentation). This rather fundamental point is often simply ignored during IIT procedures. It is therefore clear that none of them are based on rigorous capture of the actual mechanics of indentation and they differ only in

the nature of the approximations and "correction factors" involved.

A wide range of analytical formulations have been proposed for obtaining the effective values of stress and strain. These are reviewed in several publications.[23,25,26,32,33] As two particular formulations are used in the current work, their basis is now summarized here. The effective strain is commonly taken to be given by the expression originally presented by Tabor[34] in 1948.

$$\varepsilon_e = 0.2\frac{a_c}{R} \tag{1}$$

where a_c is the contact radius. The factor of 0.2, sometimes termed the "indentation strain constraint factor", is an arbitrary constant, although in fact any kind of averaged (von Mises) strain will not scale linearly with the contact radius during the plastic deformation associated with spherical indentation. Also, its most appropriate value will vary with the plasticity characteristics of the material. Nevertheless, it has often been concluded[17,26] that, for a good range of metals, this expression is as good as any similar one that might be proposed, although it is certainly true that several other formulations have been put forward.[14,26]

Of course, the value of a_c must be obtained experimentally, usually without periodically removing the load and making direct profilometry measurements. This is commonly done via measured values of load P, penetration depth h, and system stiffness S. There are several issues relating to exactly what geometrical and other assumptions are being made, as described in a number of reviews.[23,25] A typical expression for the "contact depth", h_c, is

$$h_c = h - 0.75\frac{P}{S} \tag{2}$$

This represents an attempt to account for the elastic recovery, although clearly the factor of 0.75 again constitutes some kind of arbitrary correction. The value of a_c is then obtained from this depth using the standard geometric construction of a spherical cap, giving

$$a_c = \sqrt{(2Rh_c - h_c^2)} \tag{3}$$

This allows the effective strain to be evaluated at each partial unloading point. There is then the issue of estimating the corresponding effective stress. The most common approach to this is to simply use the applied load and the projected contact area, given by

$$A_p = \pi a_c^2 \tag{4}$$

In general, it has been found that simply dividing the load by this area gives an over-estimate, so a more common expression is one with the form

$$\sigma_e = \frac{P}{2.8A_p} \tag{5}$$

The factor of 2.8, termed an "indentation stress constraint factor", also represents an arbitrary correction of some sort. Various values between about 2.5 and 3 are sometimes used.[25] As with the indentation strain constraint factor having a value of 0.2, this value of 2.8 was the one originally proposed by Tabor and it also is the one most commonly used.

In the current work, Equation (1)–(5) have been applied to experimental sets of unloading operations to give corresponding sets of points in (true) stress–strain space. This is termed "Method 1". A variant of this, based on a simpler method of evaluating a_c, has also been used, referred to here as "Method 2". Application of a Hertzian model for the unloading leads[23] to an expression for obtaining a_c directly from the measured system stiffness (without using a measured value of h)

$$a_c = \frac{S}{2E_r} \tag{6}$$

where E_r, the "reduced" Young's modulus of the sample material (considering the finite stiffness of the indenter), is given by

$$E_r = \left\{\left(\frac{1-\nu^2}{E}\right) + \left(\frac{1-\nu_i^2}{E_i}\right)\right\}^{-1} \tag{7}$$

in which ν is the Poisson ratio and the subscript i refers to the indenter. Apart from this alternative method of evaluating a_c, the equations used are the same in Methods 1 and 2.

It should finally be clarified that, as mentioned earlier (Section 1.1), most published IIT results have been obtained using nanoindenters (with either sharp or spherical indenters)—termed here "nano-IIT". However, these procedures have also been implemented using larger (spherical) indenters (mm range) and applied loads (kN range)—termed "macro-IIT". Indeed, some commercial firms, including Frontics and ABI, have offered services and/or products based on this approach for the past decade or so. Several articles[35–38] emerged from these commercial developments, although there have been very few recently. The number of what could be regarded as independent appraisals of this methodology is very limited, although a report[39] prepared by TWI is available via a subscription service. The current work includes an experimental assessment of the procedure, and a comparison with nano-IIT outcomes.

1.4. PIP Procedures

It has long been recognized that iterative FEM simulation of the indentation process, so as to converge on a best-fit set of parameter values in a constitutive law describing the stress–strain relationship, is a rigorous procedure with strong potential. Unlike the IIT procedures, no approximations are required concerning the mechanics of indentation. However, various questions surround its practicality, efficiency, and reliability. A number of publications[11–13,40–42] have addressed the issues that need to be considered. Three steps are involved in obtaining a true stress–true strain relationship via indentation: a) pushing a hard indenter into the sample with a known force, b) measuring an outcome, i.e., the (radially symmetric) profile of the indent (although most early work was based on the load-displacement plot), and c) iterative FEM simulation of the test, systematically changing the set of plasticity parameter values until optimal agreement is obtained between measured and modeled outcomes. The underlying concept is thus clear and unencumbered by uncertainty about the validity of the procedure. However, for it to be a tool of widespread utility, concerns need to be addressed

relating to the rate of convergence (in parameter space) on the "solution",[13,42–46] the possibility that it is not "unique", the resolution requirements for the experimental outcome, etc.

There are also issues relating to each individual simulation run, which include the role of interfacial friction,[47–49] the dimensions of the modeled domain, the external boundary conditions, the mesh density, etc, plus of course the execution time requirements, particularly if large numbers of runs are required in real time. Superimposed on these issues are concerns about whether a representative volume of the sample is being deformed, the optimal size of the indenter, and the effects of inhomogeneity and/or anisotropy in the sample. Also, an integrated package is clearly required, in which both the experimental measurements and the FEM simulations are under automated software control. In fact, packages of this type are now starting to become commercially available and one such facility was used in the present investigation.

1.5. Uniaxial Testing

Care must also be taken in interpretation of the outcome of conventional uniaxial testing, both tensile and compressive. In addition to potential difficulties with accurate displacement measurement, and a possible requirement for a compliance correction, it must be recognized that the standard conversion between nominal and true stress–strain relationships is only reliable if the stress and strain fields are uniform (throughout the gauge length). In tension, the onset of necking will invalidate this assumption, so it is important to be able to identify this transition. In some cases, when the initial work-hardening rate is low, this may occur at low plastic strains. It is possible to model this using FEM (for any given true stress–true strain relationship). There has been work in this area and it is accepted that predicted outcomes[50–52] should be reliable using the boundary condition of no lateral contraction at the gripped regions. Alternatively, the complete sample, including shoulder and grip regions, can be included in the simulation.

Similarly, there are complications for compressive testing, mainly concerning interfacial friction. This is commonly neglected, but in practice it is difficult to eliminate, as the contact pressure is high. A finite value for the coefficient of friction leads to barreling, which in practice is almost invariably observed. In such cases, the assumption of uniform stress and strain fields is again invalid, although it is again possible to take its effect into account via FEM modeling.[53–60] Unlike necking during tensile testing, friction during compression affects the outcome from the start. On the other hand, its effects may be relatively small, whereas necking always has a strong effect on a plot of nominal stress against nominal strain. Nevertheless, automatic conversion of nominal to true stress–strain relationships is potentially unreliable in both cases.

2. Materials and Microstructures

2.1. Materials

The following materials were included in this survey, all in the form of extruded rod: a) An OFHC Cu; b) A 6000 series Al alloy; c) A Grade C250 maraging steel (annealed, but not age-hardened).

These materials, which were supplied by Dynamic Metals (Cu and steel) and Metals Warehouse (Al), were chosen to provide a good range of plasticity characteristics. Also, there were earlier indications that they all exhibit little or no inhomogeneity or anisotropy. Test outcomes were therefore expected to be independent of how samples were prepared, or the direction of testing. This was confirmed via compression testing (Section 3.2).

2.2. Microstructure

This article does not cover microstructural issues in any detail, but there is interest in the grain structure, particularly its scale. This is associated with the question of whether the volume being deformed during the test is large enough to respond in the same way as the "bulk". This usually requires the deformed region to contain "many" grains (as many features affecting plasticity relate to grain size/shape, texture, grain boundary structures, etc, and these can only be captured by deforming an assembly of grains).

The grain structures of the three materials can be seen in **Figure 1**. These are optical images of free surfaces around (PIP) indents. (Note that, as there is a tendency for the "rim" region to be raised in a "pile-up", it is often difficult to arrange for all of the surface to be in sharp focus in an optical

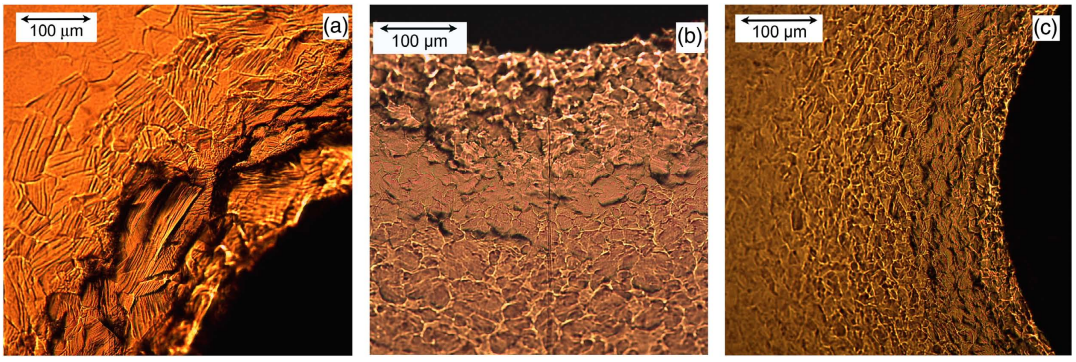

Figure 1. Optical images of regions close to indents (made with a 1 mm radius sphere) in samples of a) Cu, b) Al, c) steel. (The vertical line in the center of (b) is the trace left by a profilometer scan).

micrograph.). This is a convenient and helpful way to view the grain structure (needing no etching, polarized light, etc), as it also offers insights into how the plastic deformation has taken place. It can be seen that the grain size is around 100–200 μm for the Cu, 50–100 μm for the Al, and 10–30 μm for the steel, with all grains being approximately equiaxed. The indentation clearly involves deformation of a "many grained" volume in all cases. The IIT, however, has been carried out either with a ball radius of about 4 or 20 μm (nano-IIT) or with the same (1 mm) radius as the PIP (macro-IIT). The nano-IIT thus commonly creates deformation only in a single grain.

The sets of parallel lines seen in individual grains in Figure 1 (particularly Figure 1a) are persistent slip bands, where gliding dislocations in a particular slip system have reached the free surface. It can be seen that multiple slip systems have operated in many grains, despite the fact that the levels of plastic strain in these regions at the free surface adjacent to an indent are relatively low (≈1–2%). Furthermore, careful study often reveals evidence of grain rotations, deformation twinning, the existence of prior annealing twins, etc.

3. Testing Procedures

3.1. Tensile Testing

Conventional procedures were used, with cylindrical samples (axis parallel to extrusion direction) and threaded grips. The reduced section length was 28 mm, with 5 mm diameter. Strain measurement was done via video monitoring of the relative motion of points marked on the sample. Two sets of points were marked, with the outer pair having an initial separation of 22 mm ("long gauge length") and the inner pair a separation of 10 mm ("short gauge length"). Testing was carried out on an Instron 5569 machine, with a displacement rate of 1 mm min^{-1}. Image analysis software was used to obtain displacements from the videos, which were also used to check on the locations and evolving shapes of the necks. Three repeat runs were carried out for each material. The reproducibility of these was high.

3.2. Compressive Testing

Compression tests were carried out on all of the materials, loading in both axial and radial directions (relative to the extrusion axis). Both types of sample were short cylinders (5 mm diameter and 5 mm long). Strain was measured using a Linear Variable Displacement Transducer (LVDT), attached to the upper platen and actuated against the lower one. These tests were carried out using an Instron 3367.

3.3. IIT Testing

Background is provided in Section 1.3. The IIT tests, based on both Method 1 and Method 2, were carried out using both nanoindenters and macroscopic loading. The nanoindenters were an Anton Paar UNHT machine (load limit 100 mN), with a ball radius, R, of 4.2 μm and a MicroMaterials Nanotest Xtreme machine (load limit 400 mN), with $R = 22.5$ μm. The macro loading was done using the PLX Indentation Plastometer (Section 3.4), with a 1 mm radius ball and displacement data being acquired via an integral LVDT.

A potential issue concerns thermal drift—a common source of error with nanoindenters. Thermal drift measurements were made, with both machines. In general, there was little or no systematic drift and the maximum drift rate was found to be about 0.05 nm s^{-1}. For much of the time, it was ≈0.01 nm s^{-1}. As changes in displacement during unloading were around a few tens of nm, and measurements were made over periods of the order of a minute, errors arising from thermal drift were relatively small (compared with other sources of error such as variations in grain orientation, surface condition, etc).

3.4. PIP Testing

Some background is provided in Section 1.4. The PLX Indentation Plastometer was used in this work. Technical detail is available on the PLX website (www.plastometrex.com). Samples were mounted and polished (to 1 μm finish). They were then placed on the plinth of the plastometer and indented with a spherical indenter of radius 1 mm, made of WC–Co cemented carbide, using a force sufficient to generate a displacement (penetration) of around 200 μm (h/R ≈20%). The forces used were 1.5, 1.5, and 4.5 kN, respectively for the Cu, Al, and steel samples. A contacting stylus profilometer, with a depth resolution of about 1 μm, is incorporated into the PLX machine. Tilt correction functions were applied to the raw data, based on the far-field parts of the scan being parallel. This procedure is carried out automatically under software control.

For any approach involving iterative simulation of a deformation process, the true stress–strain relationship (material plasticity response) must be characterized via a (small) set of parameter values. Several expressions are in common use, but the current PLX methodology is based on use of the Voce equation

$$\sigma = \sigma_s - (\sigma_s - \sigma_Y)\exp\left(\frac{-\varepsilon}{\varepsilon_0}\right) \tag{8}$$

where σ is the (true) stress, ε is the (true) strain, σ_Y is the yield stress, σ_s is a saturation stress, and ε_0 is a characteristic strain (for the approach of the stress to its saturation level). When implemented in the FEM model, these stresses and strains are von Mises values.

The misfit between measured and modeled profiles is characterized by the S_{red} parameter, which has a value around 10^{-4} or below if the fit is good. Details of this, and of how convergence on the best-fit Voce parameter set is achieved, are available in the literature.[8,13] Isotropy is assumed, both elastically and plastically. The elastic constants are required as input data. The Young's moduli of the samples were taken to be 115, 70, and 200 GPa, respectively for Cu, Al, and steel samples. The Poisson ratio was taken to be 0.33 in all cases. (The outcome of the modeling is not strongly sensitive to these parameters).

4. Test Outcomes

4.1. Tensile Testing

Video stills from the end of tensile tests (immediately before fracture) on each type of material are shown in **Figure 2**. Well-defined necks formed in all cases. However, only for the Cu (Figure 2a) did it form approximately in the center of the sample. This is relevant to the post-necking parts of the stress–strain plots, which are shown in **Figure 3**. For the Cu, the neck formed within both the long (outer pair of points) and the short (inner pair of points) gauge lengths. For this material, the work-hardening rate was very low (Figure 3a) and the neck (peak in the nominal stress–strain curve) formed at very low strain (≈1%). The ductility (nominal strain at fracture) was higher (≈30%) for the short-gauge length than for the long-gauge length (≈15%). This is simply because, after the onset of necking, virtually all of the plastic straining is taking place in the neck, which constitutes a larger fraction of the gauge length for the inner pair of points than for the outer pair.

The situation is slightly different for the other two tests, where necks formed within the outer pair of points (long-gauge length), but outside the inner pair (short-gauge length). In these cases, the effect of the necking is only apparent in the long-gauge length plots, with there apparently being virtually no straining in the post-necking regime for the short-gauge length plots. In fact, the fracture strains of all three materials are similar (≈15%, for the long-gauge length plots), although this value clearly has no universal significance, as it depends on the ratio of gauge length to diameter.

Of course, most of the interest is often in the regime up to the onset of necking, particularly the yield stress and UTS values. These values are about 350 and 350 MPa, 340 and 360 MPa, and 900 and 980 MPa for the Cu, Al, and steel, respectively. However, there are at least a couple of further points to note. For example, the necking strains are a little different for the three, being respectively about 1%, 8%, and 3%. (Unlike the ductility, these values do not depend on sample dimensions.) Also, while the onset of yielding is quite sharp for the Cu and Al, there is something of a transition regime for the steel, such that the value obtained for the yield stress is likely to depend slightly on exactly how it is extracted. In any event, these three materials cover a fairly broad range in terms of their plasticity characteristics.

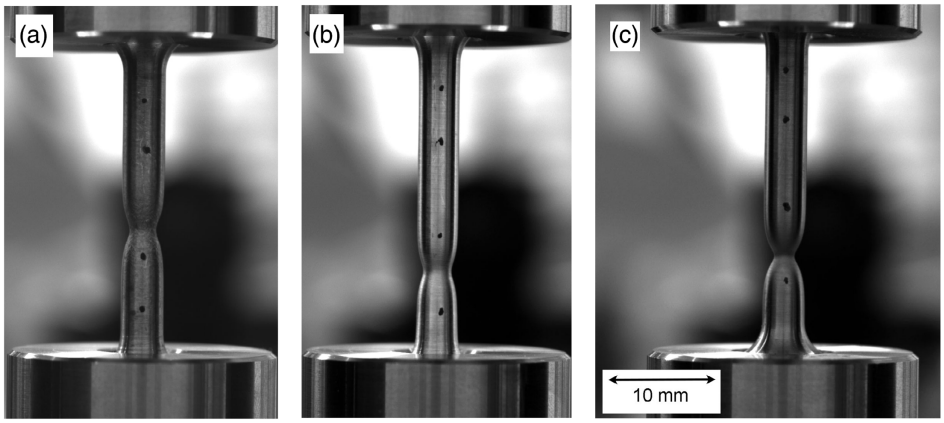

Figure 2. Stills from video recordings of tensile tests, in the post-necking regime, for samples of a) Cu, b) Al, and c) steel.

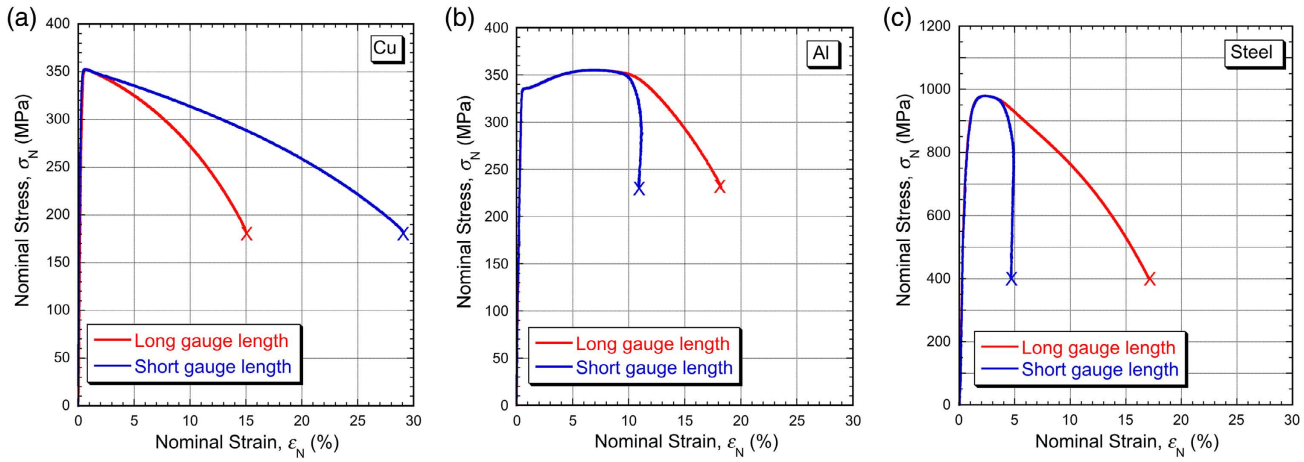

Figure 3. Plots of nominal stress against nominal strain, for the samples shown in Figure 2, made of a) Cu, b) Al, and c) steel.

4.2. Compressive Testing

The main objective here was to check whether these extruded materials exhibited any significant anisotropy (between axial and radial directions—they must be transversely isotropic). Nominal stress–strain curves are shown in **Figure 4**. Although there are indications of minor anisotropy for the Al and steel (with the axial direction being slightly harder in both cases), in general these plots confirm that they are all essentially isotropic (within about ±5%, which is a reasonable target range for any comparisons between data obtained using different methods, or even for straight repeats with a particular type of test).

4.3. Nano-IIT Testing

The raw load-displacement data from the two nanoindenters are shown in **Figure 5**, for a representative set of indents. As expected, they exhibit some scatter, although the changes in stiffness (S)—i.e., the unloading gradient—with increasing depth appear to be reasonably consistent. The final penetration ratio (h/R) is about 25% for Anton Paar and 5% for MicroMaterials. (This ratio gives a very approximate indication of the peak strains within the sample.) The strain levels being created in the sample were thus all rather small for the MicroMaterials tests.

The outcome of converting these data to a set of points in (true) stress–strain space, using Method 1 or Method 2, is shown in **Figure 6** (Anton Paar tests) and **Figure 7** (MicroMaterials tests). Several features are apparent here. One is that, with both machines, there are significant differences between the outcomes of Method 1 and Method 2, despite the fact that they are based on the same set of S measurements. Second, with the possible exception of the Anton Paar Method 1 data (Figure 6a), repeat indentation runs lead to a large scatter. This might have been expected in view of the fact that many of the indents would have been located in single grains, with their orientation expected to have a noticeable effect on the response. In fact, the maximum indent diameters were around 5 μm for both types of test, so, with a grain size of the order of 10 μm, it is likely that virtually all indents were either within a grain or straddling a couple of

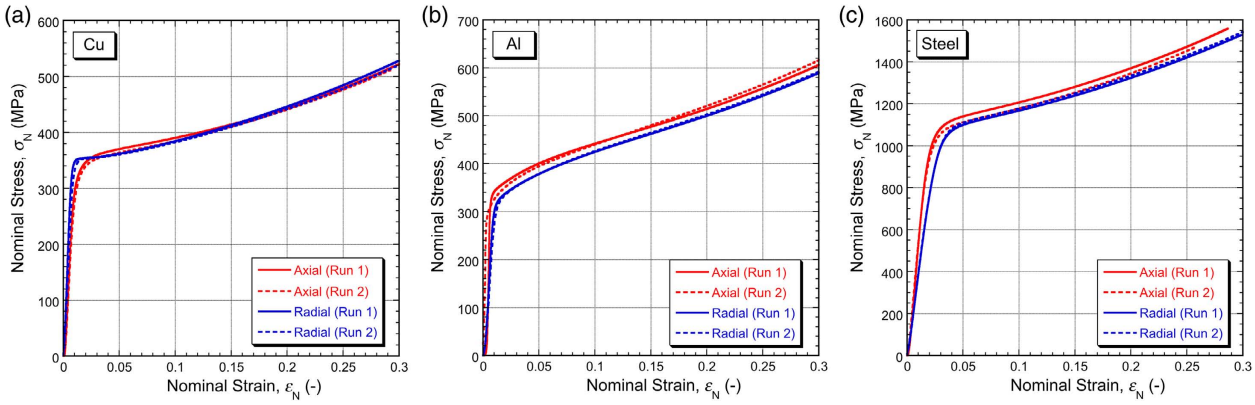

Figure 4. Plots of nominal stress against nominal strain from compression testing of a) Cu, b) Al, and c) steel.

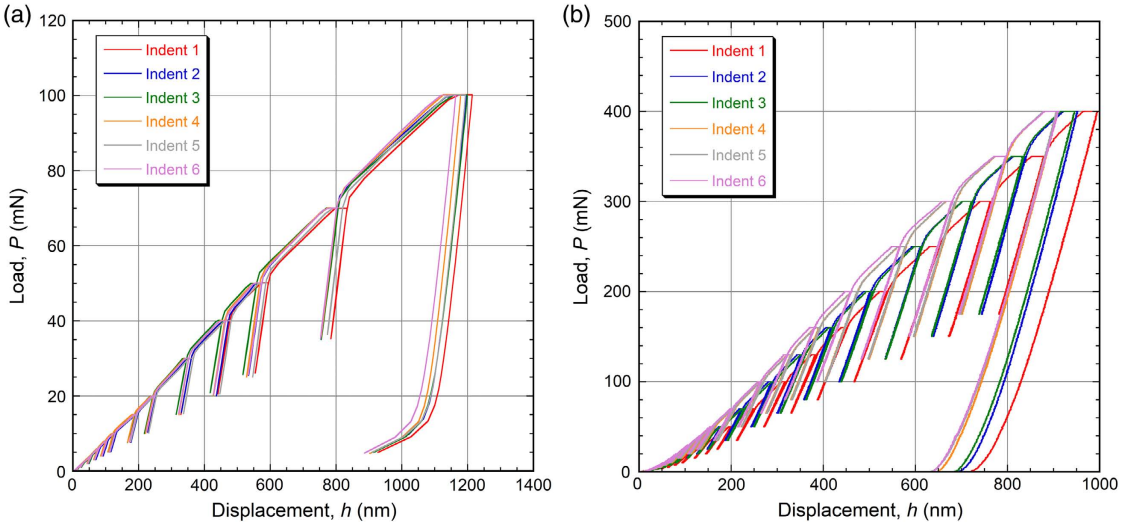

Figure 5. IIT data acquired at NPL for the steel, showing 6 plots of load against displacement, with periodic unloading operations, obtained with ball radii of: a) 4.2 μm (Anton Paar machine) and b) 22.5 μm (MicroMaterials machine).

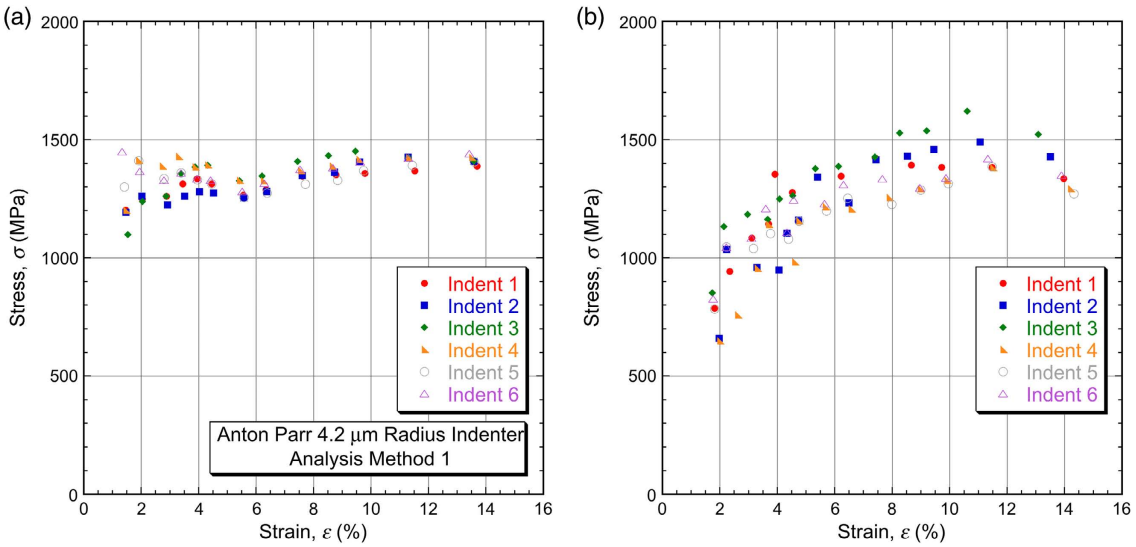

Figure 6. Points in (true) stress–strain space for the steel, obtained from the unloading gradients in Figure 5a—Anton Paar machine—via a) Method 1 and b) Method 2.

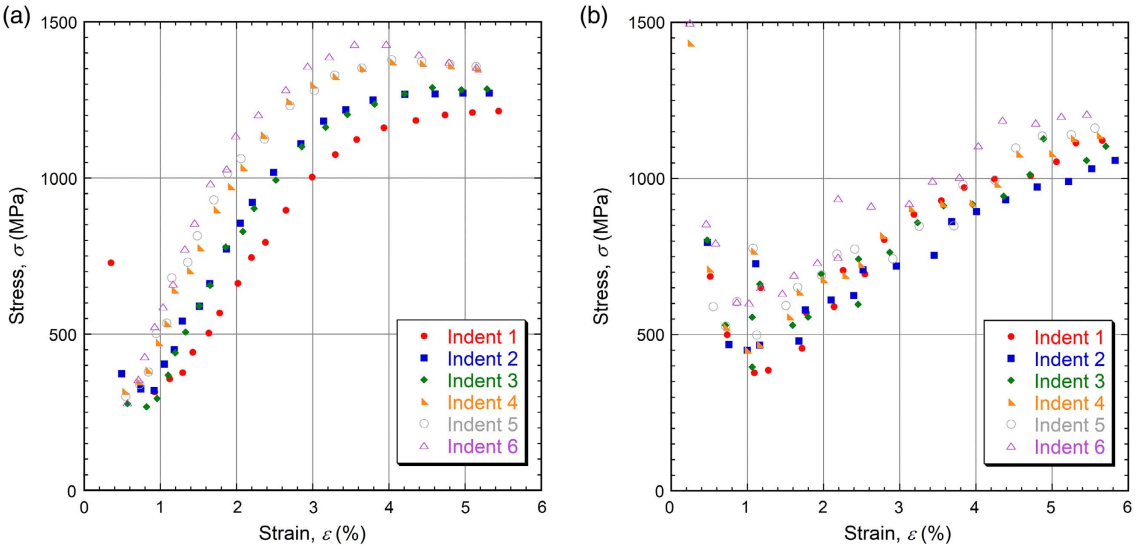

Figure 7. Points in (true) stress–strain space for the steel, obtained from the unloading gradients in Figure 5b—MicroMaterials machine—via a) Method 1 and b) Method 2.

grains. Some scatter may also have arisen from the effects of surface roughness or oxide films. One could also include in this the possibility of the metallographic preparation technique leaving a thin near-surface region with slightly different mechanical characteristics.

Moreover, while surface roughness or oxide films might be expected to introduce random noise, the response when indenting a single grain, or a pair of grains, is likely to be qualitatively different from that of a "many-grained" region. A further point to note is that the data in the initial regime (strains up to ≈1–2%) look rather inconsistent and would probably be discarded. This leaves the inferred value of the yield stress in some doubt. It would often be obtained via extrapolation from values at higher strain levels. If this were to be done, then the values obtained would be around 1100 and 600 MPa for the Anton Paar data (Methods 1 and 2, respectively), whereas the MicroMaterials data would lead to 100 and 300 MPa. These values do, of course, cover a huge range.

In any event, it is clear that this procedure gives widely different outcomes, apparently affected by the load range, the penetration depth, the variant of the method used, and even by straight repeating of a test. Moreover, in no case is the outcome at all close to that from the tensile test (for this steel). These features can be seen in **Figure 8**, in which approximated envelopes of these results are compared with the outcome of the tensile test for this steel.

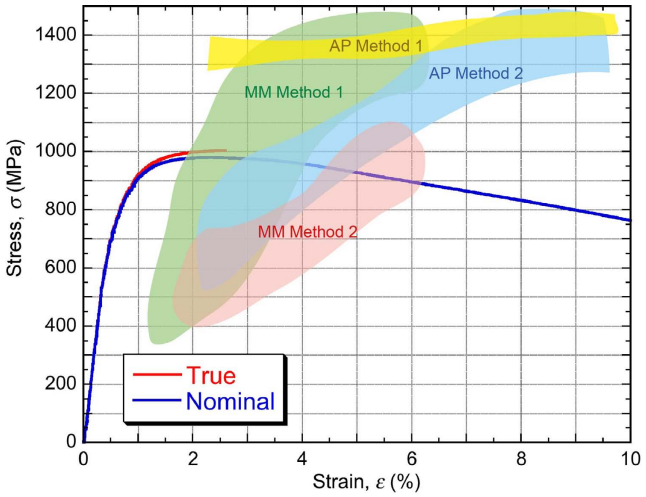

Figure 8. Comparison between the nominal stress–strain curve obtained by tensile testing of the steel (with the derived true curve also shown, up to the onset of necking) and the approximate envelopes (of true stress–true strain) obtained by applying the IIT methodology to the data from the nanoindentation tests.

4.4. Macro-IIT Testing

Corresponding (macro-IIT) outcomes, obtained using the PLX Indentation Plastometer, are shown in **Figure 9**. In this case, just a single load-displacement curve (Figure 9a) is shown, as the reproducibility was much better than for the nanoindenters. This is expected from the multigrained nature of the deformed region and the fact that penetrating to these depths (≈200 μm, compared with 1 μm for the nanoindenters) makes the outcome much less sensitive to surface roughness effects. Figure 9b shows the corresponding set of points in stress–strain space. The initial outcome (true stress–true strain) is now also shown as nominal values (for tensile loading). It can be seen that, over this strain range, the differences between the two are relatively small.

Although there is less noise, some of the features shown by the nano-IIT plots are also apparent here. For example, the outcomes from Methods 1 and 2 are substantially different, again with a tendency for the Method 2 stress levels to be lower. Also, while it could be argued that at least the Method 1 outcome is closer than for the nano-IIT to the "correct" curve (Figure 3c, i.e., a yield stress of around 900 MPa, with little work hardening), it is certainly not very accurate.

The result of applying the same procedures to the Cu and Al can be seen in **Figure 10**, which shows only nominal plots and includes comparisons with corresponding tensile test results. Certain points need to be clarified here. First, these comparisons should only be made up to the onset of necking (≈1% for the Cu and ≈8% for the Al). The subsequent drops in the tensile curves are due to neck development, which cannot be captured at all in the IIT methodology. True stress–strain curves should not normally have negative gradients and nominal ones should only be considered up to the point where the gradient falls to zero (onset of necking). Therefore, for the Cu, Method 2 is actually giving very poor predictions, despite the apparent agreement in the post-necking regime. Method 1 is better in the sense that the low rate of work hardening is being approximately captured, although the inferred yield stress, at around 500 MPa, is well above the correct value. Furthermore, for the Al the behavior is being captured reasonably well with Method 1, although in this case the yield stress would be somewhat underestimated (at ≈300 MPa) and the UTS slightly overestimated (at ≈400 MPa). Method 2 is again giving unreasonable predictions, being well below Method 1 and with a negative gradient that is clearly incorrect.

4.5. PIP Testing

Sets of indents were produced on each sample, but there were no systematic variations between different locations in individual

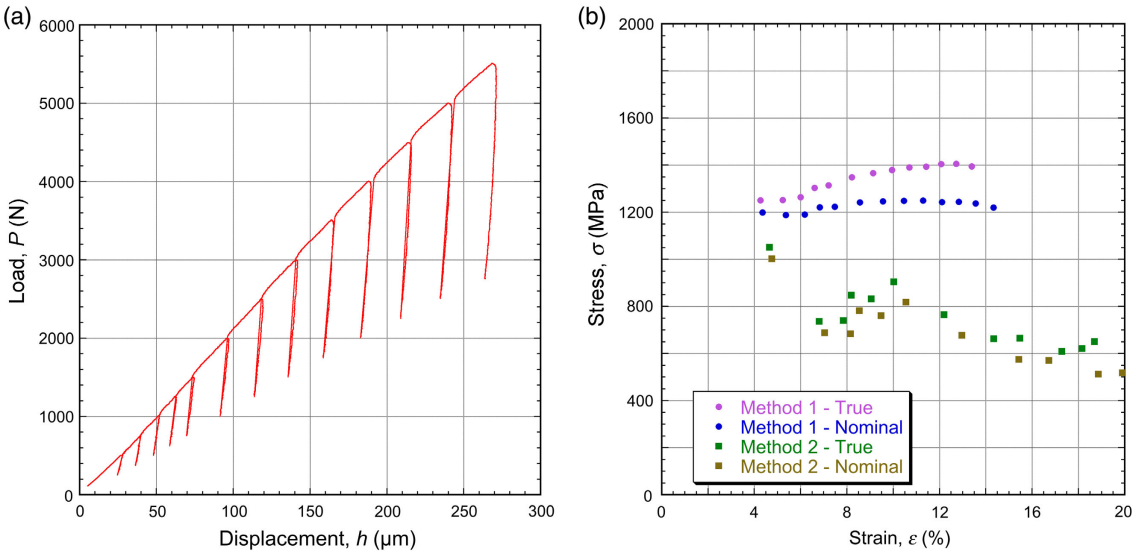

Figure 9. IIT data from "macro" loading ($R = 1$ mm) for the steel, showing a) a plot of load against displacement, with periodic unloading operations, and b) corresponding sets of points in stress–strain space, obtained using either Method 1 or Method 2.

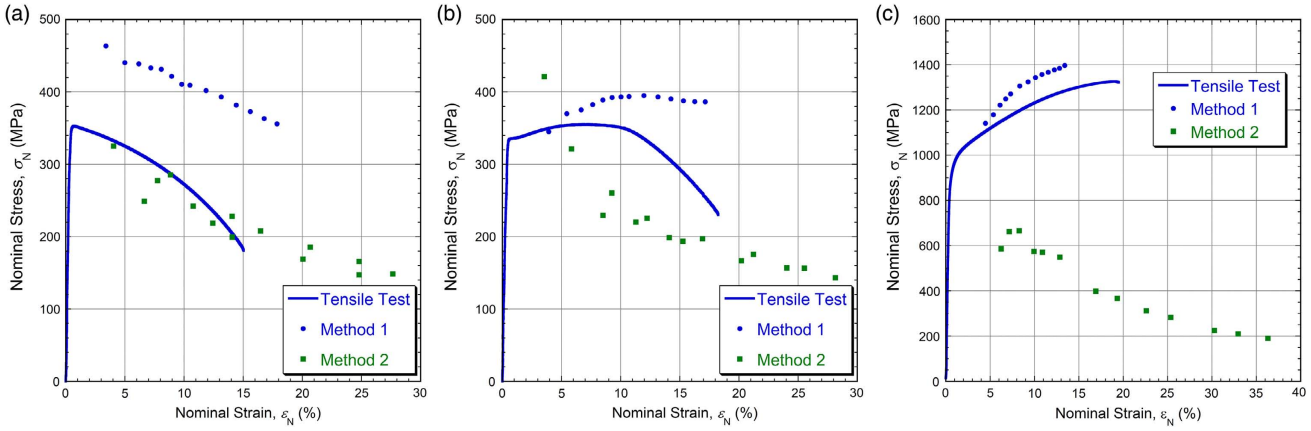

Figure 10. IIT data from "macro" loading ($R = 1$ mm), as derived sets of points in nominal stress–strain space, and compared with tensile test outcomes, obtained using either Method 1 or Method 2, for a) Cu and b) Al.

Table 1. Outcome of the PIP convergence operation on residual indent profiles (values of the parameters in the Voce equation for the true stress–true strain relationship).

Sample	Best-fit Voce parameter values		
	Yield stress σ_Y [MPa]	Saturation stress σ_s [MPa]	Characteristic strain ε_0 [%]
OFHC Cu	350	450	100
AA6000 series Al	350	550	33
Maraging steel	1000	1700	50

samples, and also that the indents were all radially symmetric, indicating that there was no significant (in-plane) anisotropy. The sets of optimized Voce plasticity parameter values are shown in **Table 1**.

The Voce relationship can be plotted, both as a true stress–strain curve and as a nominal one. The latter is derived from the former using the standard analytical equations. A nominal stress–strain curve obtained in this way is only valid while the stress and strain fields within the (gauge length of the) sample are uniform. This should be the case up until the onset of necking. Post-necking behavior in a tensile test can be predicted via FEM simulation of the test (using the inferred true stress–strain relationship). Details of this modeling are available in the literature.[8,13] Outcomes in the current cases are presented later.

Comparisons between measured and modeled profiles are shown in **Figure 11**. It can be seen that agreement is good in all cases. (There is a small discrepancy at the "rim" of the "crater" for the Cu, but this is probably due to rotation of a relatively large grain in that vicinity; such effects can create some "noise" if the grain size is fairly large, but are not an issue for these materials.) Such profiles can immediately convey certain points. For example, the pronounced "pile-up" seen for the copper is indicative of a low work-hardening rate.

An optimized set of Voce parameter values, representing a true stress–true strain curve (in the plastic regime), can be used to simulate the plastic deformation that will occur in any configuration (including a uniaxial tensile test), by running a suitable FEM model. For a tensile test, this can cover the post-necking regime and, provided a suitable fracture criterion can be

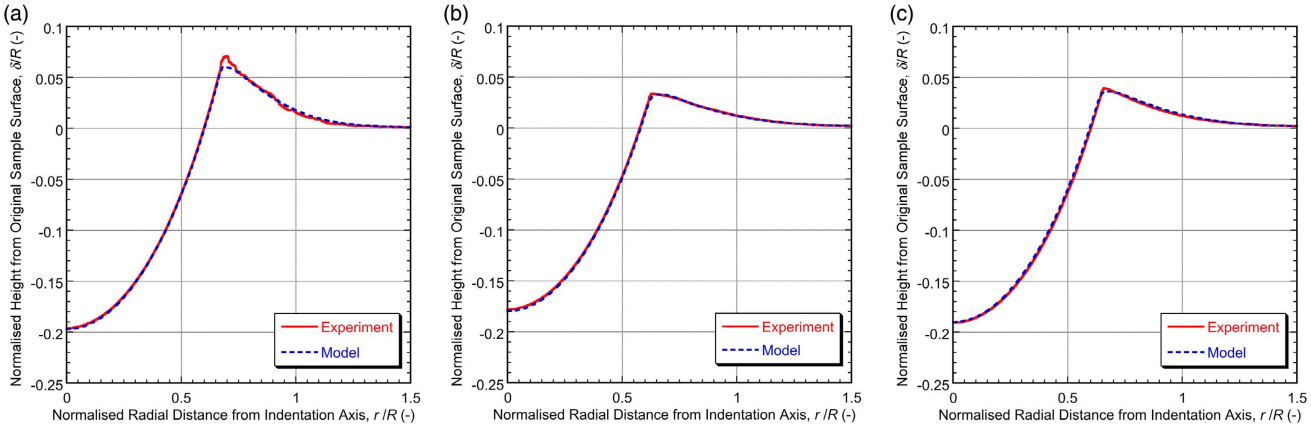

Figure 11. Comparisons between measured and (optimized) modeled residual indent profiles, for a) Cu, b) Al, and c) steel. Corresponding Voce parameter values are shown in Table 1.

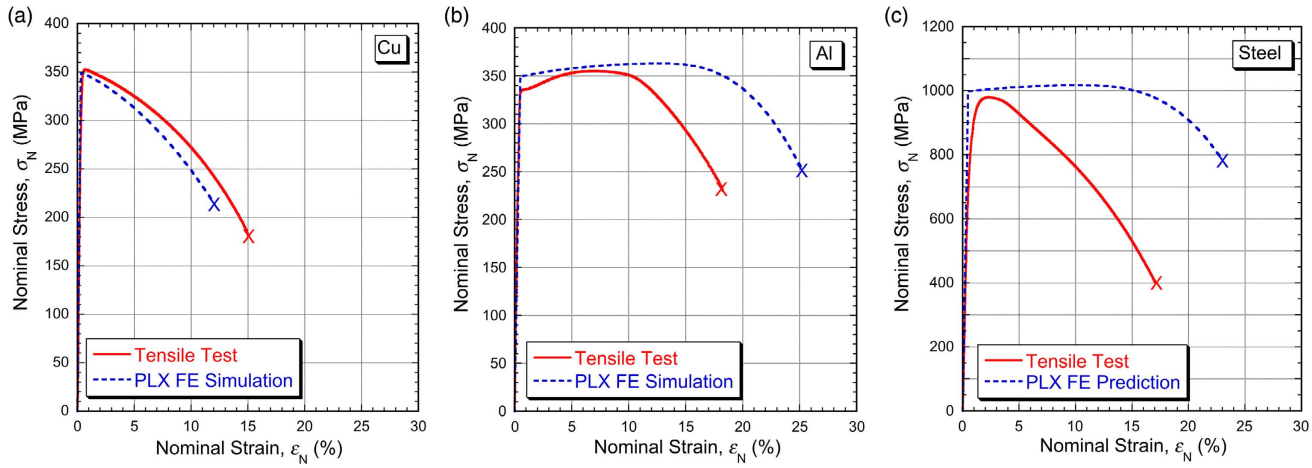

Figure 12. Comparison between tensile test outcomes (Figure 3) and curves obtained by FEM simulation of the test, using the PIP-derived true stress–strain relationship and a critical true strain at fracture of 100%, for a) Cu, b) Al, and c) steel.

identified, final failure. It has been found[8] that the peak true (von Mises) strain in the neck reaching a critical value often provides good agreement with experiment (concerning the "ductility"). The outcomes of such simulations are shown in **Figure 12** for these three materials, with corresponding tensile plots (long-gauge length cases) also shown. These plots include the elastic part of the curve.

Agreement is in general good, although it may be noted that, while the onset of plasticity (yield stress) is sharp for the Cu and Al, there is something of a transition regime (covering ≈1–2%) for the steel. Depending on exactly how the yield stress is measured, this could lead to a (small) discrepancy in yield stress values. Furthermore, with a flat plateau of the type shown by the Al and the steel, good agreement regarding the strain at the onset of necking is difficult to achieve, although the UTS value obtained is likely to be reliable. It can be seen that, for the Al and, particularly, for the steel, the necking strain is overestimated; the actual work-hardening rate is a little lower than that obtained via the PIP procedure (and the necking strain, but not the UTS, is quite sensitive to this).

Some further insights, and a general confirmation that the true stress–strain relationships are being quite well-captured in the PIP methodology, can be obtained by comparing modeled and measured neck shapes. This is done in **Figure 13**. The agreement is good for the Cu and Al, but the actual reduction in area at the neck is greater than predicted for the steel. This

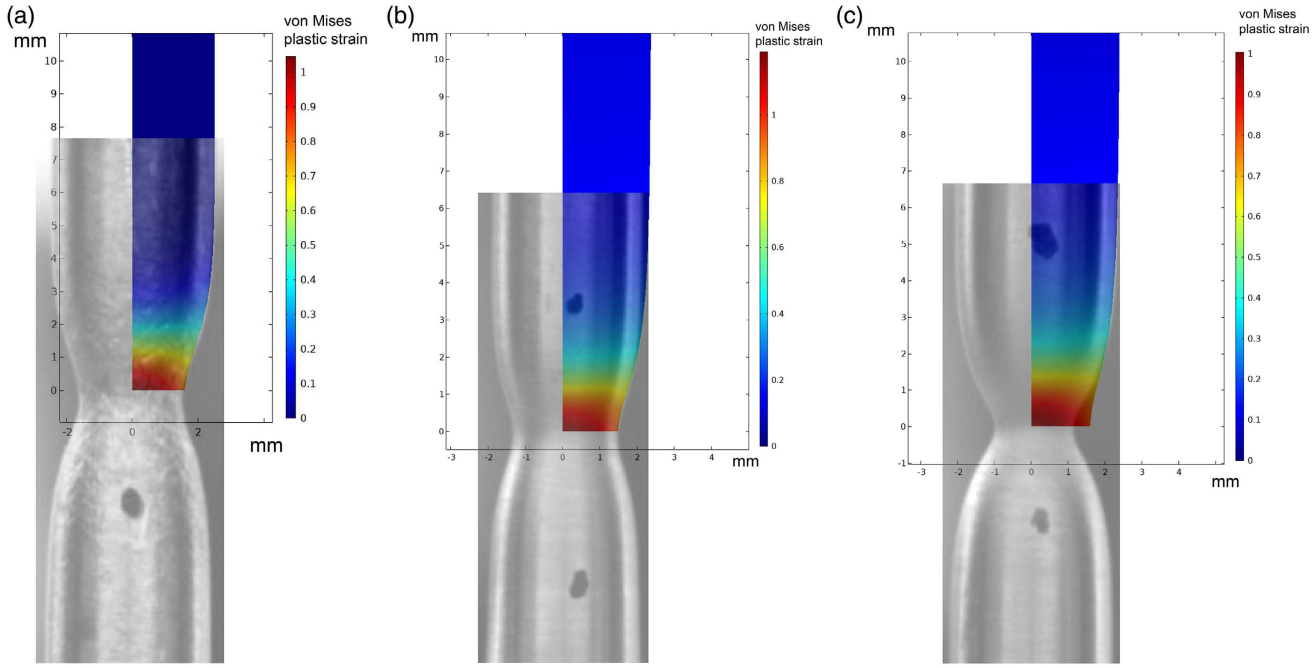

Figure 13. Superimposition of video stills of the neck region immediately before fracture during tensile tests and corresponding FEM model outcomes at that point, showing predicted neck shapes and plastic strain fields, for: a) Cu, b) Al, and c) steel.

reflects the discrepancy in the strain at the onset of necking. The FEM model is predicting uniform straining up to about 10–15%, whereas in practice necking starts at about 2–3% of (uniform) strain. This leads to a greater neck area reduction than predicted at the point where the true strain reaches 100%. Of course, different materials may in practice fracture at different true strains and in general this is unlikely to be a highly accurate fracture criterion. Overall, however, these comparisons confirm that PIP (followed by FEM modeling based on the extracted true stress–strain curve) can capture the detailed outcome of a complete tensile test quite well.

5. Conclusion

The following conclusions can be drawn from this work: a) Application to a maraging steel of two common variants of the IIT procedure, implemented using two nanoindenters, has led to inferred (true) stress–strain curves that show considerable scatter, significant differences between them, and poor agreement in all cases with that obtained via conventional tensile testing. b) A "macro" indenter has been used for IIT testing of three different materials, including the steel, with the deformed volume being suitably "multi-grained" (unlike the nanoindenter tests). This gave outcomes with reduced scatter and variability compared with those from the nano-IIT. c) Two IIT "methods" (analytical relationships) have been used. One of these gives noticeably more consistent outcomes than the other, with work-hardening rates that are in fair agreement with tensile test outcomes. Inferred values of the yield stress, however, are unlikely to be reliable. d) In contrast to these IIT outcomes, the true stress–strain curves inferred using the PIP procedure were found to be in good agreement with tensile test outcomes, regarding both yield stress and work-hardening characteristics, for all three of the metals tested. e) Good agreement was also observed between the nominal stress–strain curves, including the post-necking regimes, from tensile testing and from FEM simulation of the test, using the PIP-inferred true stress–strain curves. Moreover, this agreement extended to the shapes of the necks immediately before final rupture.

Acknowledgements

NPL acknowledge the support and funding from the Department for Business, Energy and Industrial Strategy through the Measurement for Recovery programme. T.W.C. received relevant support from EPSRC (grant EP/I038691/1) and from the Leverhulme Trust, in the form of an International Network grant (IN-2016-004) and an Emeritus Fellowship (EM/2019-038/4).

Conflict of Interest

The authors declare no conflict of interest.

Data Availability Statement

Research data are not shared.

Keywords

indentation, inverse finite element method, nanoindentation, profilometry, stress–strain curves

Received: December 16, 2020
Revised: January 20, 2021
Published online: February 16, 2021

[1] S. M. Walley, *Mater. Sci. Technol.* **2012**, *28*, 1028.
[2] E. Broitman, *Tribol. Lett.* **2017**, *65*.
[3] D. Tabor, *Philos. Mag. A* **1996**, *74*, 1207.
[4] I. M. Hutchings, *J. Mater. Res.* **2009**, *24*, 581.
[5] J. Lee, C. Lee, B. Kim, *Mater. Design* **2009**, *30*, 3395.
[6] W. Z. Yao, C. E. Krill, B. Albinski, H. C. Schneider, J. H. You, *J. Mater. Sci.* **2014**, *49*, 3705.
[7] M. Z. Wang, J. J. Wu, Y. Hui, Z. K. Zhang, X. Zhan, R. C. Guo, *Mater. Sci. Eng. A* **2017**, *679*, 143.
[8] J. E. Campbell, R. Thompson, J. Dean, T. W. Clyne, *Acta Mater.* **2019**, *168*, 87.
[9] P. Hausild, A. Materna, J. Nohava, *Mater. Design* **2012**, *37*, 373.
[10] G. Pintaude, A. R. Hoechele, *Mater. Res.* **2014**, *17*, 56.
[11] D. K. Patel, S. R. Kalidindi, *Acta Mater.* **2016**, *112*, 295.
[12] J. Dean, T. W. Clyne, *Mech. Mater.* **2017**, *105*, 112.
[13] J. E. Campbell, R. Thompson, J. Dean, T. W. Clyne, *Mech. Mater.* **2018**, *124*, 118.
[14] J. H. Ahn, D. Kwon, *J. Mater. Res.* **2001**, *16*, 3170.
[15] Y. Cao, J. Lu, *Acta Mater.* **2004**, *52*, 4023.
[16] X. Hernot, O. Bartier, Y. Bekouche, R. El Abdi, G. Mauvoisin, *Int. J. Solids Struct.* **2006**, *43*, 4136.
[17] Y. P. Cao, X. Q. Qian, N. Huber, *Mater. Sci. Eng. A* **2007**, *454*, 1.
[18] L. Y. Li, J. Z. Gu, *Int. J. Eng. Sci.* **2009**, *47*, 452.
[19] B. X. Xu, X. Chen, *J. Mater. Res.* **2010**, *25*, 2297.
[20] R. O. Oviasuyi, R. J. Klassen, *J. Nucl. Mater.* **2013**, *432*, 28.
[21] C. Yu, Y. H. Feng, R. Yang, G. J. Peng, Z. K. Lu, T. H. Zhang, *J. Mater. Res.* **2014**, *29*, 1095.
[22] Z. Song, K. Komvopoulos, *Mech. Mater.* **2014**, *76*, 93.
[23] S. Pathak, S. R. Kalidindi, *Mater. Sci. Eng. R-Rep.* **2015**, *91*, 1.
[24] J. S. Weaver, S. R. Kalidindi, *Mater. Design* **2016**, *111*, 463.
[25] C. Chang, M. A. Garrido, J. Ruiz-Hervias, Z. Zhang, L. L. Zhang, *Adv. Mater. Sci. Eng.* **2018**, 2018.
[26] F. Pohl, *Exp. Tech.* **2018**, *42*, 343.
[27] T. R. Zhang, S. Wang, W. Q. Wang, *Results Phys.* **2018**, *8*, 716.
[28] N. Huber, C. Tsakmakis, *J. Mech. Phys. Solids* **1999**, *47*, 1569.
[29] A. H. Mahmoudi, S. H. Nourbakhsh, R. Amali, *J. Test. Eval.* **2012**, *40*, 211.
[30] K. Jeong, H. Lee, O. M. Kwon, J. Jung, D. Kwon, H. N. Han, *Mater. Design* **2020**, *196*, 15.
[31] L. Lu, M. Dao, P. Kumar, U. Ramamurty, G. E. Karniadakis, S. Suresh, *Proc. Natl. Acad. Sci. U.S.A.* **2020**, *117*, 7052.
[32] T. H. Zhang, P. Jiang, Y. H. Feng, R. Yang, *J. Mater. Res.* **2009**, *24*, 3653.
[33] Y. Li, P. Stevens, M. C. Sun, C. Q. Zhang, W. Wang, *Int. J. Mech. Sci.* **2016**, *117*, 182.
[34] D. Tabor, *Proc. R. Soc. A* **1948**, *192*, 247.
[35] K. W. Lee, K. H. Kim, J. Y. Kim, K. H. Kim, B. H. Choi, D. Kwon, *J. Loss Prev. Process Ind.* **2009**, *22*, 868.
[36] E. C. Jeon, J. S. Park, D. S. Choi, K. H. Kim, D. Kwon, *J. Eng. Mater. Technol.-Trans. ASME* **2009**, *131*, 6.
[37] S. K. Kang, J. Y. Kim, C. Park, H. U. Kim, D. Kwon, *J. Mater. Res.* **2010**, *25*, 337.
[38] A. S. Hamada, F. M. Haggag, D. A. Porter, *Mater. Sci. Eng. A* **2012**, *558*, 766.

[39] A. Motarjemi, J. Speck, *Inspectioneering J.* **2005**.
[40] C. Heinrich, A. M. Waas, A. S. Wineman, *Int. J. Solids Struct.* **2009**, *46*, 364.
[41] J. Dean, J. M. Wheeler, T. W. Clyne, *Acta Mater.* **2010**, *58*, 3613.
[42] L. Meng, P. Breitkopf, B. Raghavan, G. Mauvoisin, O. Bartier, X. Hernot, *Int. J. Mater. Forming* **2018**, *12*, 587.
[43] J. Isselin, A. Iost, J. Golek, D. Najjar, M. Bigerelle, *J. Nucl. Mater.* **2006**, *352*, 97.
[44] S. Swaddiwudhipong, J. Hua, E. Harsono, Z. S. Liu, N. S. B. Ooi, *Modell. Simul. Mater. Sci. Eng.* **2006**, *14*, 1347.
[45] I. Peyrot, P. O. Bouchard, R. Ghisleni, J. Michler, *J. Mater. Res.* **2009**, *24*, 936.
[46] J. Chen, H. N. Chen, J. Chen, *Acta Metall. Sin.* **2011**, *24*, 405.
[47] A. E. Giannakopoulos, S. Suresh, *Scr. Mater.* **1999**, *40*, 1191.
[48] B. Taljat, G. M. Pharr, *Int. J. Solids Struct.* **2004**, *41*, 3891.
[49] V. Karthik, P. Visweswaran, A. Bhushan, D. N. Pawaskar, K. V. Kasiviswanathan, T. Jayakumar, B. Raj, *Int. J. Mech. Sci.* **2012**, *54*, 74.
[50] H. S. Kim, S. H. Kim, W. S. Ryu, *Mater. Trans.* **2005**, *46*, 2159.
[51] E. I. Samuel, B. K. Choudhary, K. B. S. Rao, *Mater. Sci. Eng. A* **2008**, *480*, 506.
[52] Z. P. Guan, *Mater. Design* **2014**, *56*, 209.
[53] Z. H. Yao, D. Q. Mei, H. Shen, Z. C. Chen, *Tribol. Lett.* **2013**, *51*, 525.
[54] J. Zhou, P. He, J. F. Yu, L. J. Lee, L. G. Shen, A. Y. Yi, *J. Vac. Sci. Technol. B* **2015**, *33*.
[55] X. Wang, H. Li, K. Chandrashekhara, S. A. Rummel, S. Lekakh, D. C. Van Aken, R. J. O'Malley, *J. Mater. Process. Technol.* **2017**, *243*, 465.
[56] M. Fardi, R. Abraham, P. D. Hodgson, S. Khoddam, *Adv. Eng. Mater.* **2017**, *19*.
[57] M. Bol, R. Kruse, A. E. Ehret, *J. Mech. Behav. Biomed. Mater.* **2013**, *27*, 204.
[58] G. Torrente, *Mater. Res.-Ibero-Am. J. Mater.* **2018**, *21*.
[59] X. G. Fan, Y. D. Dong, H. Yang, P. F. Gao, M. Zhan, *J. Mater. Process. Technol.* **2017**, *243*, 282.
[60] D. Duran, C. Karadogan, *Strojniski Vestnik-J. Mech. Eng.* **2016**, *62*, 243.